



Article ID 1007-1202(2022)03-0218-13

DOI <https://doi.org/10.1051/wujns/2022273218>

Optimal Control Virtual Inertia of Optical Storage Microgrid Based on Improved Sailfish Algorithm

□ LIAO Hongfei¹, ZENG Guohui^{1†}, HUANG Bo¹,
MA Chi¹, CHEN Gong¹, ZHAO Jinbin²

1. School of Electronic and Electrical Engineering, Shanghai University of Engineering Science, Shanghai 201620, China;

2. College of Power Engineering, Shanghai University of Electric Power, Shanghai 200090, China

© Wuhan University 2022

Abstract: The optical storage microgrid system composed of power electronic converters is a small inertia system. Load switching and power supply intermittent will affect the stability of the direct current (DC) bus voltage. Aiming at this problem, a virtual inertia optimal control strategy applied to optical storage microgrid is proposed. Firstly, a small signal model of the system is established to theoretically analyze the influence of virtual inertia and damping coefficient on DC bus voltage and to obtain the constraint range of virtual inertia and damping coefficient; Secondly, aiming at the defect that the Sailfish optimization algorithm is easy to premature maturity, a Sailfish optimization algorithm based on the leak-proof net and the cross-mutation propagation mechanism is proposed; Finally, the virtual inertia and damping coefficient of the system are optimized by the improved Sailfish algorithm to obtain the best control parameters. The simulation results in Matlab/Simulink show that the virtual inertia control optimized by the improved Sailfish algorithm improves the system inertia as well as the dynamic response and robustness of the DC bus voltage.

Key words: optical storage microgrid; virtual inertia; damping coefficient; improved Sailfish optimization algorithm; optimal control

CLC number: TP 305

Received date: 2022-03-10

Foundation item: Supported by the National Natural Science Foundation of China (52177184)

Biography: LIAO Hongfei, male, Master candidate, research direction: DC microgrid intelligent control. E-mail: 15900935728@qq.com

† To whom correspondence should be addressed. E-mail: zenggh@sues.edu.cn

0 Introduction

Digital technology is leading the development and evolution of the Fourth Industrial Revolution and promoting industrial digital transformation. Promoting the deep integration of advanced digital technologies and power grids is an important way for the digital transformation of power grids^[1,2]. The shortage of fossil energy and environmental problems have accelerated the development of new power technologies for distributed generation based on renewable energy^[3]. The rapid development of microgrids has laid the physical foundation for the digital transformation of energy, interconnectivity, and mesh coverage^[4,5]. At present, on the power generation side, the output of mainstream photovoltaic units and energy storage units are all direct current (DC); on the power consumption side, the high-frequency devices in the market, such as electric vehicles, mobile phones, and LEDs, are all DC loads. In the optical storage microgrid, there is no need to consider issues such as phase and reactive power, and the high-frequency DC-DC converter greatly reduces the space. The construction of the optical storage microgrid can effectively reduce the conversion loss of electric energy in the converter, and provide a great physical help for the development of the digital microgrid. The optical storage microgrid system composed of power electronic converters is a small inertial system. The load switching in the system and the intermittent power output will lead to violent fluctuations in the DC bus voltage, which in turn affects the safe and stable operation of the microgrid system^[6]. The energy

storage unit in the microgrid plays an important role in stabilizing the bus voltage of the DC microgrid^[7]. Appropriate control improvements on the basis of the droop control can effectively enhance the inertial support of the DC microgrid system. Virtual synchronous generator control (VSG) provides inertial support for the system by simulating the rotor characteristics of traditional synchronous motors. At present, the application research of this control in the alternating current (AC) system has been relatively mature.

Wu *et al.*^[8] proposed a virtual inertia control strategy for bidirectional grid-connected converters of DC microgrid by analogy with the virtual inertia of AC microgrid. This strategy can effectively solve the stability problem caused by constant power load, but its control parameters are not adaptive. In the process of digitalization of the power grid, intelligent control is an important part. In order to realize the intelligent control of the control parameters, Ren *et al.*^[9] used the voltage fluctuation rate as a function variable, and carried out an adaptive function design for the virtual inertia and damping coefficient; Yang *et al.*^[10] added the voltage deviation to the adaptive function variable; Karimi *et al.*^[11] used fuzzy control to adaptively design the virtual inertia and damping coefficient. The above self-adaptive design is obtained from the analysis of the voltage fluctuation curve of the system disturbance. This method has fuzzy characteristics. It can only be adjusted by experience in the simulation project, and it is difficult to achieve digital accuracy.

Swarm intelligence optimization algorithm is a powerful tool to provide solutions to complex problems by simulating the behavior of some special groups in nature, and it has been widely used in many fields^[12-15]. Injecting intelligent algorithms into VSG control can inject vitality into the development of digital power grids. Li *et al.*^[16] used the multi-objective particle swarm optimization algorithm to obtain the optimal inertia and damping coefficient of VSG control in AC system; Cheng *et al.*^[17] added the elimination mechanism to optimize the particle swarm optimization, which further improved the accuracy of particle swarm optimization; Yao *et al.*^[18] proposed a virtual inertia control based on neural network. Different from the engineering experience dependence of fuzzy control, the virtual inertial parameter design is realized by means of intelligent algorithm, which makes the virtual inertial control more accurate. However, the intelligent virtual inertial control of the above intelligent

algorithm is applied to the AC system. This paper takes the bidirectional DC/DC converter with the energy storage unit connected to the optical storage microgrid as the research subject, obtains the virtual inertial control suitable for the bidirectional DC/DC converter through the analogy of the virtual inertial control of the AC system, then uses the improved AC sailfish optimization algorithm (ACSFO) to optimize virtual inertia and damping coefficients. Firstly, a small-signal model is established, and the stability constraints of the virtual inertia and damping coefficient are analyzed by means of the transfer function Bode diagram; Secondly, the sailfish algorithm is improved by integrating the anti-leakage net strategy and the vertical and horizontal crossover variation propagation mechanism, and the validity of the algorithm is verified and analyzed by using the high-dimensional test function. After verification, the improved sailfish optimization algorithm is used to obtain the optimal solution of virtual inertia and damping coefficient. Finally, the optimal control strategy of virtual inertia and damping coefficient based on the improved sailfish algorithm proposed in this paper is simulated by Matlab/Simulink, then the simulation results are used to verify its effectiveness and the correctness of theoretical analysis.

1 Optical Storage Microgrid Structure and VSG Control

1.1 Optical Storage Microgrid Structure and Control Strategy

Figure 1 shows the topology of the optical storage microgrid studied in this paper, which is mainly composed of photovoltaics, energy storage units, AC loads, DC loads and corresponding power electronic converters. The whole system uses the DC bus as the medium to exchange energy through the corresponding power electronic converters. The inverter connected to the photovoltaic unit uses maximum power point tracking to make full use of the new energy. The AC and DC loads are connected to the DC bus through a one-way voltage reducer. The energy storage unit is connected to the DC bus through a bidirectional DC/DC converter. The equivalent circuit diagram of the converter is shown in Fig. 2. The converter adopts VSG control and uses the improved sailfish algorithm to improve the virtual inertia and damping coefficient to achieve optimal control, which can improve system inertia as well as the dynamic

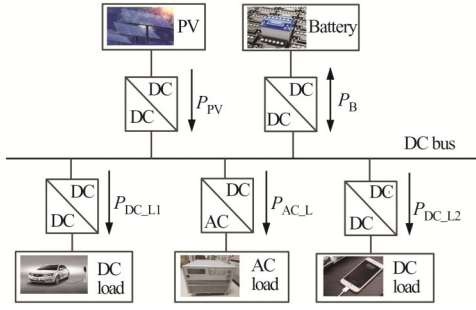


Fig. 1 Topology of DC microgrid

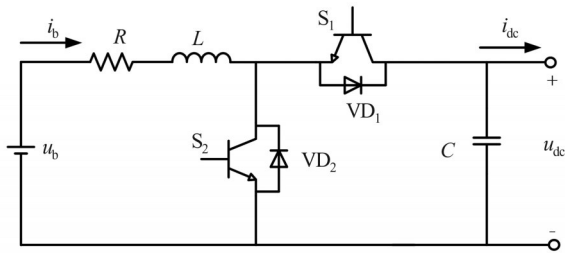


Fig. 2 Bidirectional DC-DC converter equivalent circuit diagram

R : equivalent resistance; L : filter inductance; u_{dc} : DC bus voltage; i_{dc} : the converter output current; C : voltage regulator capacitor

response of DC bus voltage.

1.2 The Principle of VSG Control

The active power-frequency control of the VSG in the inverter in the AC system is to improve the inertia of the system by simulating the rotor motion characteristics of the synchronous generator. The specific expression obtained from the simulation is

$$P_{ref} - P_0 - D(\omega - \omega_n) = J \frac{d\omega}{dt} \quad (1)$$

where P_{ref} , P_0 are the reference active power and output power, ω , ω_n are the angular frequency and rated angular frequency, and D , J are the damping coefficient and virtual inertia, respectively. According to the control analogy analysis of the AC system and the DC system in Ref. [13], the corresponding relationship of the parameters can be obtained, as shown in Table 1.

According to the parameter correspondence in Table 1, the virtual inertia control of the bidirectional

Table 1 Correspondence of VSG control parameters of DC system compared with AC system

DC/AC inverter with VSG	DC/DC converter
ω	u_{dc}
P_0	i_{dc}
J	C_v

DC/DC converter applied to the optical storage microgrid can be obtained, and its expression is

$$i_{ref} - i_{dc} - D_v(u_{dc}^* - u_{ref}) = C_v \frac{du_{dc}^*}{dt} \quad (2)$$

where i_{ref} is the reference output current, C_v and D_v are the virtual inertia and damping coefficient respectively, u_{dc}^* is the reference value of the DC bus voltage, and u_{ref} is the rated value of the DC bus voltage. The bidirectional DC/DC converter connected to the energy storage unit adopts the control method of formula (2), which can increase the inertia and damping characteristics on the basis of the droop control. When the DC bus voltage changes suddenly, the virtual inertia C_v can quickly simulate the output current and enhance the inertial support of the system. When the DC bus voltage unit is changed, D_v describes the active power change of the control output, and the damping coefficient can speed up the recovery of the DC bus voltage.

The bidirectional DC/DC virtual inertial control block diagram of the optical storage microgrid established according to the VSG control is shown in Fig. 3. Its control consists of three parts: droop control, virtual inertia control and voltage and current double closed-loop control to stabilize the DC bus voltage.

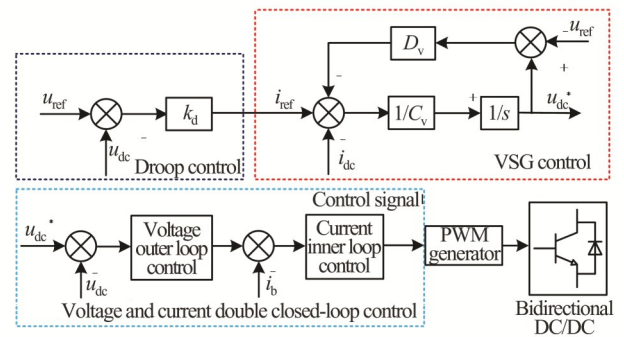


Fig. 3 Virtual inertial control block diagram

k_d : droop coefficient; i_b : output current of the energy storage unit

2 Stability Constraint Analysis

2.1 Small Signal Modeling

In order to obtain the optimal configuration of virtual inertia and damping parameters through the ACSFO algorithm, a small-signal model is established for the scenario where VSG control is applied to a bidirectional DC/DC converter. Constraints of relevant control parameters are obtained by small signal analysis.

According to Fig. 2, the small signal model of the bidirectional DC/DC converter is

$$\begin{cases} sC\hat{u}_{dc}(s) = (1-D)\hat{i}_b(s) - I_b\hat{d}(s) - \hat{i}_{dc}(s) \\ sL\hat{i}_b(s) = \hat{u}_b(s) - R\hat{i}_b(s) - (1-D)\hat{u}_{dc}(s) + U_{dc}\hat{d}(s) \end{cases} \quad (3)$$

where \hat{u}_{dc} , \hat{i}_b , \hat{d} , \hat{i}_{dc} , \hat{u}_b are the disturbance of the DC bus voltage u_{dc} , the output current of the energy storage unit i_b , the duty cycle d , the output current of the converter i_{dc} , and the output voltage of the energy storage unit u_b , respectively; and U_{dc} , I_b , D are the steady-state values of u_{dc} , i_b , d , respectively.

From formula (3), after substituting the steady-state operating point, its system transfer function is

$$\begin{cases} G_{id} = \frac{U_{dc}/R_L + sCu_{dc}}{s^2CL + sCR + (1-D)^2} \\ G_{vd} = \frac{u_{dc}(1-D) - \frac{u_{dc}(sL+R)}{R_L(1-D)}}{s^2CL + sCR + (1-D)^2} \end{cases} \quad (4)$$

where R_L is the load resistance value.

2.2 PI Parameter Setting

In order to eliminate the influence of the proportional-integral (PI) parameters of the controller on the stability, it is necessary to design the PI parameters of the voltage and current double closed-loop control. The proportional and integral parameters of the current inner loop are k_{ip} , k_{ii} , and the current inner loop compensation function is $G_i = k_{ip} + k_{ii}/s$. The proportional and integral parameters of the voltage outer loop are k_{vp} , k_{vi} , and the voltage outer loop compensation function is $G_v = k_{vp} + k_{vi}/s$. The switching frequency of the converter is 50 kHz, and the cut-off frequency of the current loop is set to 20% of the switching frequency. The obtained Bode diagram of the current inner loop correction is shown in Fig. 4.

The designed current inner loop PI values are

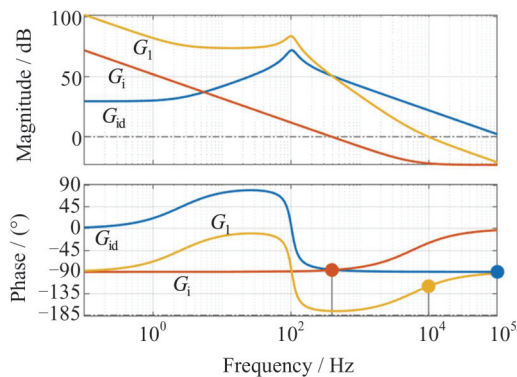


Fig. 4 Bode diagram of current inner loop correction

G_i : the current inner loop compensation function; G_{id} : Bode diagram before compensation; G_i : Bode diagram after compensation

0.068 02 and 2 467.4, respectively. It can be seen from Fig. 4 that the crossover frequency after system correction is 10 kHz, and the phase angle margin is 60° , which meets the requirements of the system stability.

The cut-off frequency of the voltage loop is set to 4% of the switching frequency, and the resulting Bode diagram of the voltage outer loop correction is shown in Fig. 5.

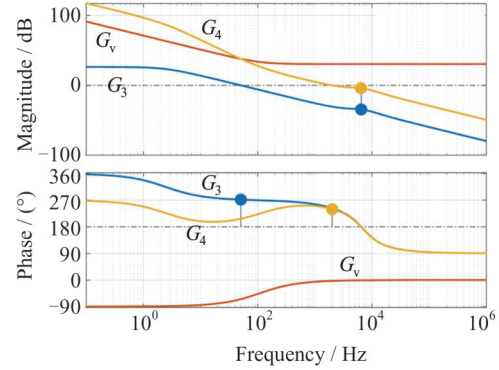


Fig. 5 Bode diagram of voltage outer loop correction

G_v : the voltage outer loop compensation function; G_3 : Bode diagram before compensation; G_4 : Bode diagram after compensation

The designed voltage outer loop PI values are 32.881 8 and 22 431.8, respectively. It can be seen from Fig. 5 that the crossover frequency after system correction is 2 kHz, and the phase angle margin is 60° , which meets the requirements of the system stability.

2.3 Virtual Inertia and Damping Coefficient Stability Constraints

From Eq. (4), we can know that the small signal model of the VSG equation is:

$$\hat{u}_{dc}^* = \frac{-\hat{i}_{dc}}{sC_v + D_v} \quad (5)$$

From Fig. 3, the transfer function of the output voltage deviation to the output current deviation after adding VSG control can be obtained as:

$$G_5 = \frac{G_i G_{id} G_{vd} G_v}{G_{id} (sC_v + D_v) (1 + G_i G_{id})} \quad (6)$$

Substituting Table 4 and the designed double closed-loop PI value into the transfer function can obtain the Bode diagram when the virtual inertia and damping coefficient change, as shown in Fig. 6 and Fig. 7.

From Fig. 6, when D_v increases within a certain interval, its phase margin decreases and the system cut-off frequency decreases, so the increase of the damping coefficient will reduce the system stability. When $D_v = 30$,

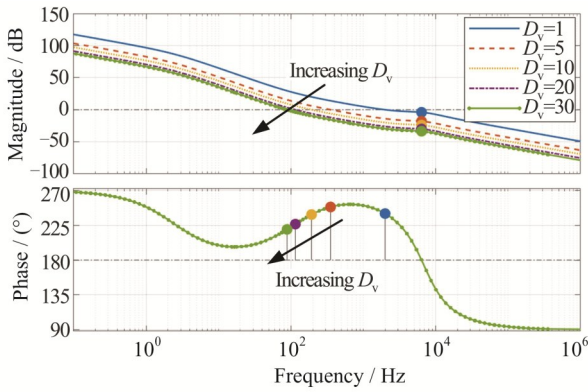


Fig. 6 Bode diagram with D_v changed

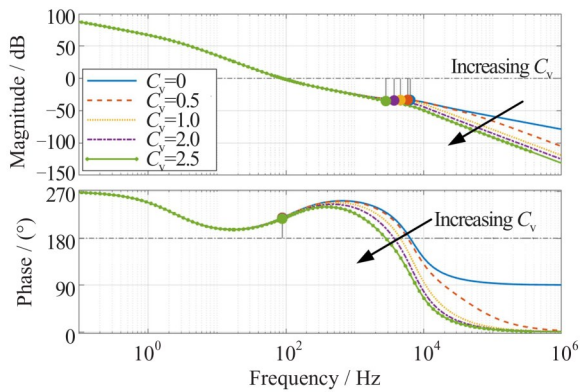


Fig. 7 Bode diagram with C_v changed

the phase margin is 39.6° . In engineering, the phase margin is generally 40° to 60° as the system stability criterion.

From Fig. 7, when C_v increases within a certain interval, its phase margin remains unchanged, and the system cut-off frequency remains unchanged, which does not affect the system stability. Therefore, the increase of virtual inertia within a certain range will not reduce the system stability. However, if the virtual inertia exceeds a certain value, the phase margin will decrease rapidly and the system will become unstable.

For the virtual inertia and damping coefficient, the limit range of the phase margin of 40° to 60° in engineering can be used as a constraint for the subsequent optimization of the algorithm to ensure its stability.

2.4 Droop Coefficient Stability Constraint

It can be seen from Fig. 3 that the transfer function of output voltage deviation to output current deviation under simultaneous droop control is

$$G_6 = k_d \frac{G_i G_{id} G_{vd} G_v}{G_{id} (s C_v + D_v) (1 + G_i G_{id})} \quad (7)$$

where k_d is the droop coefficient. It can be seen from the

above formula that as k_d increases, both the virtual inertia and the damping coefficient are reduced. It can be seen from Fig. 5 that if the damping coefficient is too low, the phase margin will be reduced, and the system will become unstable. Considering the need to improve the inertial support and stable operation of the system, a smaller droop coefficient should be selected. Considering the current power limit of the converter and the fluctuation range of the DC bus voltage, the design formula of the droop coefficient is

$$k_d = \frac{i_{\max}}{\Delta u_{dc_m}} \quad (8)$$

where i_{\max} is output maximum current for the converter, and Δu_{dc_m} is the maximum value of DC bus voltage fluctuation. The output current of the converter is limited by its capacity, and a better droop coefficient can be designed by using formula (8).

3 Sailfish Optimization Algorithm and Its Improvement

3.1 Basic Sailfish Optimization Algorithm

The sailfish algorithm simulates the alternate hunting of sailfish in groups of sardines^[19]. First, the sardine and sailfish populations are randomly initialized; Second, the sailfish uses the attack alternately to break the collective defense of the sardines; Finally, the sailfish catches suitable sardines through hunting to complete the position optimization.

1) Sailfish location update

Sailfish adopts the method of attack substitution in the hunting process, and learns in coordination with each other during the attack process. The position update formula is as follows:

$$X_{\text{newSF}}^i = X_{\text{eliteSF}}^i - \lambda_i \times (\text{rand}(0, 1) \times (\frac{X_{\text{eliteSF}}^i + X_{\text{injuredS}}^i}{2}) - X_{\text{oldSF}}^i) \quad (9)$$

where X_{oldSF}^i is the current position of the sailfish, X_{newSF}^i is updated position for sailfish, and X_{eliteSF}^i is elite sailfish that the closest to the prey with the best fitness, X_{injuredS}^i is injured sardine with optimal fitness, $\text{rand}(0, 1)$ is a random number from 0 to 1, and λ_i is the iteration coefficient of the i -th iteration as in formula (10)

$$\lambda_i = 2 * \text{rand}(0, 1) * \text{PD} - \text{PD} \quad (10)$$

where PD is the prey density, and its variation formula is

$$\text{PD} = 1 - (\frac{N_{\text{SF}}}{N_{\text{SF}} + N_{\text{S}}}) \quad (11)$$

where N_{SF} , N_S are the numbers of sailfish and sardines, respectively. The number of sailfish is expressed as:

$$N_{SF} = N * \text{Percent} \quad (12)$$

where N is the total number of sailfish and sardine populations, and Percent is the proportion of sailfish in the total population.

2) Sardine location update

When the sardine is attacked, its position update formula is:

$$X_{\text{newS}}^i = r * (X_{\text{eliteSF}}^i - X_{\text{oldS}}^i + AP) \quad (13)$$

where X_{oldS}^i , X_{newS}^i are the current and updated positions of the sardines, respectively, r is a random number from 0 to 1, and AP is the best attack power for sailfish. The attack power of the sailfish will decrease with the number of iterations, which is expressed as:

$$AP = A * (1 - 2 * t * e) \quad (14)$$

where t is the current number of iterations, and A and e control the conversion of attack power. The attack strength changes linearly from A to 0, and the reduction of the sailfish attack strength can speed up the convergence. When $AP > 0.5$, we should update all the positions of the sardines with formula (5); when $AP < 0.5$, we should update the sardine section location. Locations are represented as:

$$\alpha = N_S * AP \quad (15)$$

$$\beta = d_i * AP \quad (16)$$

where α is the number of sardines to update, β is the number of dimensions to update, and d_i is the number of variables.

3) Predation stage

During the final phase of the hunt, sardines injured by a sailfish attack during an iteration are quickly caught by the sailfish, in which the sailfish will update to the sardine's location as soon as it kills the sardine. Its position update formula is as follows:

$$X_{SF}^i = X_S^i \quad \text{if } f(S_i) < f(SF_i) \quad (17)$$

where X_{SF}^i , X_S^i are the current positions of sailfish and sardines, and $f(SF_i)$, $f(S_i)$ are the fitness of sailfish and sardines, respectively.

3.2 Improvement of Sailfish Optimization Algorithm

Compared with other swarm intelligence algorithms, the sailfish algorithm has good convergence speed and optimization accuracy, but it is easy to lag and fall into a local optimal state during the convergence process. In order to speed up the convergence, improve optimization accuracy, and enhance the optimal configura-

tion effect for virtual inertia and damping coefficient, the following three improvement methods are proposed.

1) Cubic mapping initializing the population

Population initialization affects the convergence speed and accuracy of the algorithm. Using random numbers to generate the initialized population does not have good ergodicity, and the population will appear local aggregation, which will affect the performance of the algorithm. Cubic mapping is conducted with excellent maximum Lyapunov exponent and excellent ergodic performance. Its expression is as follows:

$$x_{n+1} = \rho x_n (1 - x_n^2), \quad \rho \in (1.5, 3), x_n \in (0, 1) \quad (18)$$

where ρ is the control parameter. In mapping, x_0 takes a random number between 0 and 1. Experimental analysis shows that the best condition is $\rho = 2.95$. The simulation is performed according to formula (18), and the simulation results are shown in Fig. 8. Compared with random distribution, the sequence distribution generated based on Cubic mapping is more uniform.

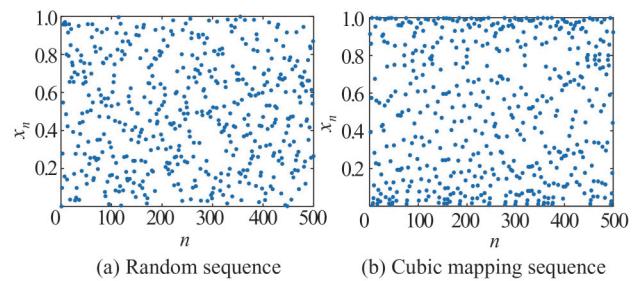


Fig. 8 Sequence release diagram generated by different methods

2) Anti-leakage net strategy based on self-triggering mechanism

Sailfish keeps approaching the injured individual sardines during the iterative process and attacks them in a single way during the hunting process. During predation, some fast-moving sardines could not avoid escaping, which leads to the premature maturity of the algorithm; and as the number of iterations of the algorithm increases, sailfish populations will gather around the current optimal solution, causing the algorithm's falling into a local optimum.

In order to improve the predation efficiency of sailfish and avoid getting stuck in local optima, this paper proposes a self-triggering mechanism of the anti-leakage net strategy. After the sailfish is updated according to formula (9), the anti-leakage net strategy is used to perturb the position of the sailfish. The expression of the anti-leakage net strategy is as follows:

$$X_{\text{newSF}}^i = \begin{cases} r_1 * (\text{ub} - \text{lb}) + \text{lb} & (r_2 < \beta) \\ p * X_{\text{oldSF}}^i & (r_2 > \beta) \end{cases} \quad (19)$$

where r_1, r_2 is a random number from 0 to 1, ub, lb are the upper and lower bounds of the search space, respectively, p is a scaling factor that decreases linearly from 1 to 0 with the number of iterations, and β is the expansion factor.

In formula (19), when $r_2 < \beta$, we reinitialize the current individual, expand the search range of the sailfish population in the global space, prevent sardines from escaping the encirclement, and prevent the algorithm from falling into local optimum. When $r_2 > \beta$, the individual sailfish will move to the vicinity of the current position in the proportion of p , get rid of the attraction of some sardines in a small range, and jump out of the local extreme value. The linearly decreasing p combines the characteristics that the sailfish algorithm needs a large-scale search in the early stage of iteration and a small-scale fine-scale search in the later stage of the iteration, which enhances the algorithm's optimization ability.

In the anti-leakage net strategy, it will reinitialize the current individual when $r_2 < \beta$. The larger the value of β , the greater the probability of re-initialization, and it is difficult to avoid the decrease of the algorithm solving efficiency at this time. In order to solve the problem that the fixed β value leads to the decrease of algorithm solving efficiency, this paper adopts a dynamically changing β , and the formula is as follows:

$$\beta = 0.1 + 0.4 \times \frac{t}{T} \quad (20)$$

where β will increase with the increase of the number of iterations, so the anti-leakage net strategy will move proportionally with a greater probability in the early stage of the iteration, and the anti-leakage net will increase the probability of re-initialization accordingly in the later stage of the iteration so as to avoid the decline of population diversity.

Considering that adopting the anti-leakage net strategy in each iteration will increase the running burden of the algorithm, a self-triggering mechanism is embedded to improve the burden of running the algorithm. Its expression is:

$$\gamma = (\gamma_{\max} - \gamma_{\min}) - (\gamma_{\max} - \gamma_{\min}) \times (1 - (\frac{t}{T})^\delta)^{\frac{1}{\delta}} \quad (21)$$

where $\gamma_{\max}, \gamma_{\min}$ are the maximum value and the minimum value of the trigger factor γ , respectively (The preset maximum is 0.8 and the minimum is 0.2). When the random number is $\text{rand}(0, 1) < \gamma$, the anti-leakage net strat-

egy is triggered; otherwise, the anti-leakage net strategy is not used. $\delta (\delta \geq 1)$ is the adjustment factor.

The self-triggering curve is shown in Fig. 9. Compared with the linear increment ($\delta = 1$), the nonlinear increment method ($\delta > 1$) has a slow growth of the γ value and a lower trigger probability in the initial stage of the algorithm iteration, which ensures the convergence speed in the early stage of the iteration. In the later stage of the iteration, γ becomes larger and grows rapidly, and the trigger probability increases. At this time, the sailfish will escape from the local extreme value space through the anti-leakage net strategy so as to avoid falling into the premature algorithm in the later stage of the iteration. The degree of concaveness of the nonlinear increasing function can be adjusted by δ . If the algorithm appears premature, δ can be appropriately reduced to improve the trigger probability in the early stage of iteration and avoid the algorithm from falling into local optimum.

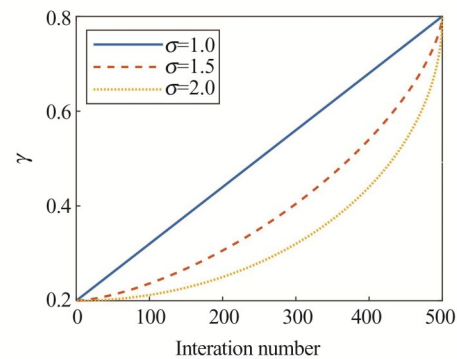


Fig. 9 Relationship between trigger factor and iteration number

3) Cross mutation propagation mechanism

To further adapt the algorithm to complex environments and to fully improve its global development ability and local exploration ability, this paper proposes a cross-mutation propagation mechanism to improve the sailfish search method through the horizontal cross-information propagation mechanism to allow sufficient information dissemination among individuals, and at the same time refers to elite individual information to avoid blind learning among individuals, which ensures the optimization efficiency while improving the optimization accuracy. The vertical cross-variation is to carry out cross-variation in different dimensions of the individual so as to prevent the individual from falling into the local optimum due to a stagnant dimension, and to improve

the activity of the population and the ability to jump out of the local optimum.

The horizontal cross information dissemination mechanism can effectively allow two individuals (i and j) to learn from each other and produce high-quality offspring. The specific improved crossover operation is as follows:

$$\text{MSX}_{\text{oldSF}}^{i,d} = r_3 * X_{\text{oldSF}}^{i,d} + (1 - r_3) * X_{\text{oldSF}}^{j,d} + c_1 * \left(\frac{X_{\text{oldSF}}^{j,d} + X_{\text{eliteSF}}^{i,d}}{2} - X_{\text{oldSF}}^{i,d} \right) \quad (22)$$

$$\text{MSX}_{\text{oldSF}}^{j,d} = r_4 * X_{\text{oldSF}}^{i,d} + (1 - r_4) * X_{\text{oldSF}}^{j,d} + c_2 * \left(\frac{X_{\text{oldSF}}^{i,d} + X_{\text{eliteSF}}^{j,d}}{2} - X_{\text{oldSF}}^{j,d} \right) \quad (23)$$

where $\text{MSX}_{\text{oldSF}}^{i,d}$, $\text{MSX}_{\text{oldSF}}^{j,d}$ are the d -dimension individuals generated by the sailfish individual $X_{\text{oldSF}}^{i,d}$, $X_{\text{eliteSF}}^{i,d}$ and the reference sailfish elite individual, r_3 , r_4 are random numbers from 0 to 1, and c_1 , c_2 are random numbers of $[-1,1]$. The individuals generated by the horizontal crossover operation need to be preserved with the parent.

The vertical crossover operation mainly mutates one of the dimensions, allowing the dimensions to learn from each other so as to avoid the parental individual from falling into a local optimum due to the stagnation of a certain dimension. The specific mutation methods are as follows:

$$\text{MSX}_{\text{oldSF}}^{i,d} = r_5 * X_{\text{oldSF}}^{i,d_1} + (1 - r_5) * X_{\text{oldSF}}^{i,d_2} \quad (24)$$

where $\text{MSX}_{\text{oldSF}}^{i,d}$ is the offspring individual generated by d_1 and d_2 of the individual through longitudinal variation; r_5 is a random number between 0 and 1. The progeny and parent of the longitudinal variation are preferentially preserved. Through the preferential mechanism, the optimal dimension information in the individual sailfish can be retained and the stagnant dimension information can be removed to improve the population diversity.

The excellent individual information generated by the vertical mutation will be spread to other individuals

through the horizontal crossover operation, and the activity of the whole population will be improved. The cross-optimization of the population through the cross-mutation propagation mechanism improves the activity of the population, enhances the ability to jump out of the local optimum, and further improves the convergence speed and the performance of solving complex optimization problems.

3.3 ACSFO Algorithm Optimization Test

In order to test the effect of ACSFO algorithm on function optimization, this paper compares ACSFO algorithm with 4 classical intelligent algorithms (Particle Swarm Optimization (PSO) algorithm, Multi-Verse Optimizer (MVO) algorithm, Grey Wolf Optimizer (GWO) algorithm, Moth-flame optimization (MFO) algorithm) and the original sailfish optimization algorithm SFO in 4 typical test functions. The optimization is carried out in the test function. The four groups of test functions are shown in Table 2. The F_1 and F_3 test functions are shown in Fig. 10. The population size is 30, the dimension is set to 30, and the maximum number of iterations is set to 500 times. In order to avoid randomness, each algorithm is optimized 30 times. Taking the average fitness value of 30 calculations as the ordinate, and the number of iterations as the abscissa, the function convergence curve is shown in Fig. 11.

Table 2 Test function

Test function	Test dimension	Search scope	Optimal solution
Sphere (F_1)	30	$[-100,100]$	0
Rosenbrock (F_2)	30	$[-30,30]$	0
Rastrigin (F_3)	30	$[-5.12,5.12]$	0
Griewank (F_4)	30	$[-600,600]$	0

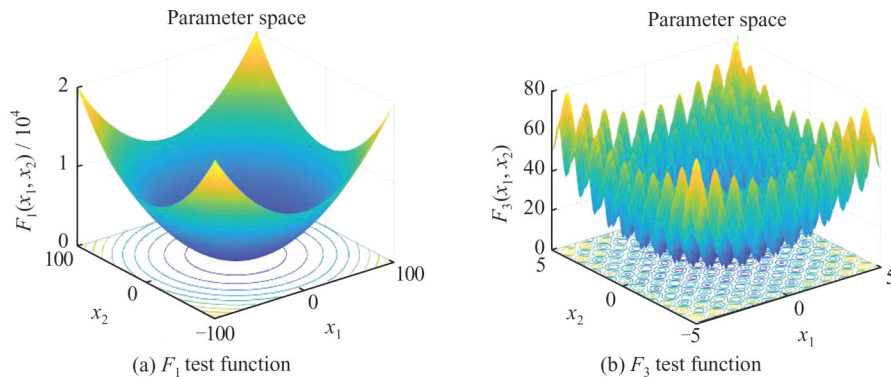


Fig. 10 Test function graph

It can be seen from Fig. 10 that F_1 is a multi-dimensional single-peak test function, which can test the global optimization ability of the algorithm, and F_3 is a multi-dimensional multi-peak test function, which can test the algorithm's ability to jump out of the local optimum.

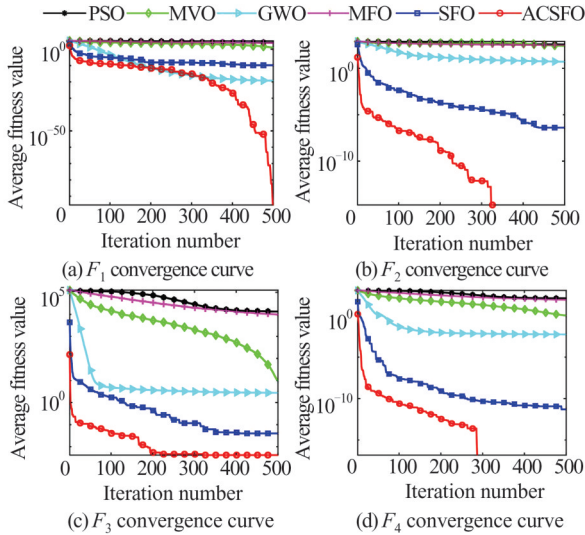


Fig. 11 Convergence curves of test functions under different algorithms

From the convergence curves of F_1 , F_2 , F_3 and F_4 , it can be seen that, ACSFO has a great improvement in convergence speed and optimization accuracy compared with SFO. From F_2 , F_3 , and F_4 , it can be clearly seen that the initialization of the population based on the Cubic map makes the generated initial value closer to the optimal solution and improves the diversity of the search space. F_1 , F_2 , F_3 , and F_4 found the optimal solution, indicating that after introducing the anti-leakage net strategy based on the self-triggering mechanism, the sailfish can expand the hunting range during the alternate hunting process, enhance the sailfish search ability, and avoid falling into the local optimum. It can be seen from F_1 , F_2 and F_4 that in the later stage of the iteration, there is a tendency to fall into the local optimum. The addition of the horizontal cross-propagation mechanism makes the convergence speed faster, and the addition of the vertical cross-mutation makes the stagnant dimension jump out of the local area. It can be clearly seen from F_3 and F_4 that the algorithm stagnates at 300 and 290 iterations respectively, and vertical cross-mutation avoids the defect of dimensional iteration stagnation, and then quickly finds the optimal solution.

It can be seen that the ACSFO algorithm has a great

improvement in the SFO algorithm, and its convergence speed and optimization accuracy are improved. Compared with other classical intelligent algorithms, it also has very superior optimization performance.

4 Improvement of VSG Control Based on ACSFO Algorithm

4.1 Fitness Function Design

The fitness function used to evaluate the position of the particle can guide the search direction of the algorithm, and plays a key role in the optimization algorithm to meet the convergence accuracy and convergence speed of the system.

In this paper, the integral of time multiplied by absolute value of error (ITAE) is adopted as the performance optimization objective of microgrid system. Its expression is:

$$\text{ITAE} = \int_0^t |e(t)| dt \quad (25)$$

where $e(t)$ is the output error. Taking ITAE as the fitness function can make the transient response oscillation of the system smoother and the voltage followability strong.

In order to improve the inertial support of the microgrid system, obtain the optimal virtual inertia and damping coefficient, enhance the smoothness of the transient response of the system, and follow the voltage, the designed fitness function is:

$$\text{fitness} = \int_0^t |\Delta u_{dc}(t)| dt \quad (26)$$

where fitness is the fitness function value of the population, and $\Delta u_{dc}(t)$ is the deviation of the DC bus voltage.

4.2 ACSFO Algorithm Flow Design

The main logic and flow of the ACSFO algorithm to improve virtual inertial control are shown as follows.

ACSFO algorithm flow

- 1) Parameter initialization: sailfish population size, sardine population size, iteration times
- 2) Chaos initialization population
- 3) Calculate and sort the fitness values of sailfish and sardine respectively according to formula (26). Pick the best position in the two populations and record its position.
- 4) while $t < T$
- 5) for $i = 1$ to N_{sf}
- 6) Calculate γ according to formula (21)
- 7) if $r_i > \gamma$
- 8) Update the sailfish position according to formula (9)

-
- 9) end if
 - 10) Calculate β according to formula (20)
 - 11) if $r_1 < \gamma$
 - 12) Update the sailfish position according to formula (19)
 - 13) end if
 - 14) end for
 - 15) if (AP<0.5)
 - 16) for $i = 1$ to α
 - 17) Update the sardine position according to formula (13)
 - 18) end for
 - 19) else
 - 20) for $i = 1$ to N_s
 - 21) Update the sardine position according to formula (13)
 - 22) end for
 - 23) end if
 - 24) Calculate the fitness values of sailfish and sardine populations separately
 - 25) for $i = \min(N_{SF}, N_S)$
 - 26) if sardine fitness value < sailfish fitness value
 - 27) Sardine sailfish position swap
 - 28) end if
 - 29) end for
 - 30) Initialize the removed sardine position
 - 31) Calculate the fitness value of sardines, complete the sorting of sailfish and sardines according to the fitness value, and compare the two groups with each other to record the optimal individual
 - 32) for $i=1: N_{SF}/2$
 - 33) Get the i -th pair of laterally propagated individuals
 - 34) for $d = 1$ to D
 - 35) According to formulas (22) and (23), calculate the offspring formed by horizontal cross-propagation, and compare with their parents to leave outstanding individuals
 - 36) end for
 - 37) end for
 - 38) for $i=1: D/2$
 - 39) for $j=1: N_{SF}$
 - 40) Calculate the offspring formed by longitudinal variation according to formula (24), and compare with their parents to leave outstanding individuals
 - 41) end for
 - 42) end for
 - 43) $t = t+1$
 - 44) end while
-

5 Simulation Results

In order to verify the effectiveness of the improved sailfish algorithm proposed in this paper for the virtual inertia optimal control strategy and the correctness of the theory, the optical storage microgrid model shown in Fig. 1 is built in Matlab/Simulink, and the photovoltaic adopts the Maximum Power Point Tracking (MPPT) control. The bidirectional DC/DC converter connected to the battery grid adopts different control strategies according to the needs. The corresponding system parameters are shown in Table 3.

Table 3 System parameters

Project	Parameter
Photovoltaic modules	Rated temperature $T_N=25^\circ$
	Rated irradiance $I_r=1\ 000\ \text{W/m}^2$
	Rated capacity $P_N=4\ 000\ \text{W}$
Battery	Rated voltage $U_{bN}=160\ \text{V}$, rated capacity $50\ \text{A}$
Photovoltaic one-way converter P-DC	$L_c=5\ \text{mH}$, $C_c=3\ 300\ \mu\text{F}$
Energy storage bidirectional converter B-DC	$L=0.5\ \text{mH}$, $C=200\ \mu\text{F}$
Load	$R_L=6\ \Omega$

Figure 12 describes the effect of virtual inertia on the optical storage microgrid. The blue curve only adopts droop control, and the droop control means that we should set virtual inertia $C_v=0$. For the rest of the curves, the damping coefficient is set to 20, and the virtual inertia is a variable. Figure 12(a) describes the voltage dynamic response. When the reference voltage changes, the voltage rapidly changes to the voltage reference value in the droop control case; in the VSG control case, the voltage changes slowly to the voltage reference value, and the system inertial support is significantly improved. As the virtual inertia increases, the voltage changes more slowly, the inertial support is stronger, and the voltage quality improves. Figure 12(b) shows the influence of load power mutation on the DC bus voltage. Similarly, as the virtual inertia increases, the inertial support is stronger and the fluctuation is weakened. When $t=1\ \text{s}$, the load power suddenly increases by 5 kW, at this time, the VSG control will reduce the power delivered to the microgrid; when $t=1.5\ \text{s}$, the load power will sud-

denly drop by 5 kW, and the VSG control will increase the power delivered to the microgrid and enhance the inertial support of the microgrid.

Figure 13 describes the effect of the damping coefficient on the optical storage microgrid, setting the virtual inertia $C_v=0$ and the damping coefficient D_v as a variable. Figure 13(a) depicts the voltage dynamic response. In the case of VSG control, as the damping coefficient increases, the voltage response is faster and the deviation from the reference voltage is smaller, but it also reduces a certain inertia. In Fig. 13(b), when $t=1$ s, the load power suddenly increases by 5 kW, and when $t=1.5$ s, the load power suddenly drops by 5 kW. In the two cases of sudden change, with the increase of the damping coefficient, the deviation is smaller and the recovery of stable values is faster.

Through theoretical and simulation analysis, we can know that the larger the virtual inertia, the stronger the inertial support of the system, which avoids the violent fluctuation of the DC bus voltage, but at the same time the voltage recovery speed becomes slower. The larger the damping coefficient, the higher the voltage response speed, but the damping coefficient will have a certain weakening effect on the inertia. At the same time, it can be seen from the theoretical analysis in Fig. 6 that the damping coefficient is too large which will af-

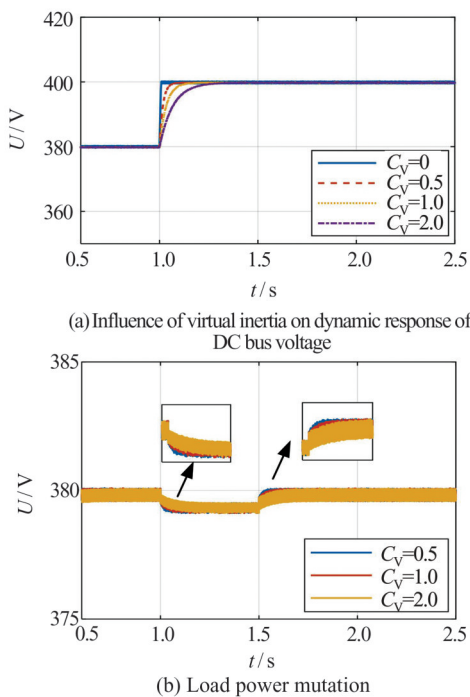


Fig. 12 Influence of virtual inertia on optical storage DC microgrid

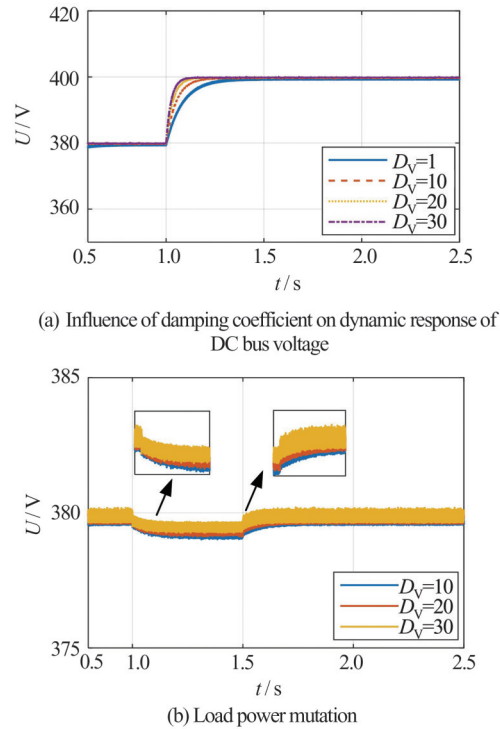


Fig. 13 Influence of damping coefficient on optical storage DC microgrid

fect its stability. In order to realize the optimal solution of virtual inertia and damping coefficient of VSG control, formula (26) is used as the fitness function, and the ACSFO algorithm is used to find the optimal solution of parameters. The value ranges of the virtual inertia and damping coefficient are set to $[0, 2.5]$ and $[0, 30]$, respectively, the number of algorithm population is 20, and the number of iterations is 50. The iteration curve is obtained as shown in Fig. 14.

It can be seen from Fig. 14 that the ACSFO algorithm has a great improvement over the original SFO algorithm, showing great advantages in finding the optimal, and its convergence speed and convergence accu-

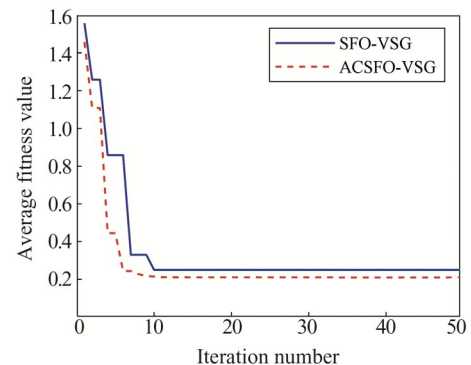


Fig. 14 Iterative curve diagram of algorithm

racy are greatly improved in the original SFO algorithm.

When the load power changes, the simulation comparison diagram of the optimal configuration of virtual inertial control using the ACSFO algorithm is shown in Fig. 15.

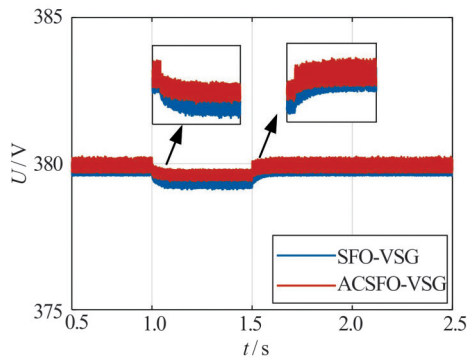


Fig. 15 DC bus voltage fluctuation curve under different control

It can be seen from Fig. 15 that the ACSFO algorithm has better dynamic response ability, shorter recovery time and smaller fluctuation than the SFO algorithm.

6 Conclusion

In order to promote the digitization process of the power grid, this paper uses an intelligent method to solve the voltage quality problem caused by the low inertia of the DC microgrid. Firstly, by analogy with the DC/AC inverter with VSG, the VSG control is applied to the DC bidirectional DC/DC converter of the optical storage microgrid. After that, the anti-leakage net strategy and the cross-mutation propagation mechanism are integrated into the Sailfish optimization algorithm to improve the global optimization ability. Finally, an intelligent optimization control strategy of virtual inertia and damping coefficient is proposed.

Through theoretical analysis and experimental verification, the following conclusions are drawn:

1) The low inertia problem of the DC microgrid is effectively solved by constructing a VSG control strategy, and the voltage following performance is enhanced. Using ACSFO algorithm to realize the configuration of VSG control parameters can effectively improve its system adaptability and intelligence. Effectively using ITAE as a fitness function can take into account its error accuracy and convergence speed at the same time in parameter configuration, which can improve the following performance while enhancing the inertial support of the

system, and provide ideas for the acquisition of electrical data in digital power grids.

2) The ACSFO algorithm integrates the anti-leakage network strategy and the vertical and horizontal crossover mutation propagation mechanism, which enhances the global development ability and local exploration ability of the SFO algorithm, greatly improves the algorithm optimization accuracy and convergence speed. By using the ACSFO algorithm, the optimal configuration of the VSG control parameters can be achieved.

3) This paper only aims to add VSG control based on ACSFO algorithm to the bidirectional DC/DC converter in a single optical storage microgrid, and does not consider the coordinated control of the intelligent microgrid system with mesh interconnection of the optical storage microgrid. The insufficiency of this paper is also the future research direction.

References

- [1] Bai H, Zhou C C, Yuan Z Y, *et al.* Prospect and thinking of digital power grid based on digital twin [J]. *Southern Power System Technology*, 2020(8): 18-24(Ch).
- [2] Li P, Xi W, Cai T T, *et al.* Concept, architecture and key technologies of digital grid [J]. *Chinese Journal of Electrical Engineering*. DOI: 10.13334/j.0258-8013.pcsee.212086 (Ch).
- [3] Adib A, Fateh F, Mirafzal B. Smart inverter stability enhancement in weak grids using adaptive virtual-inductance [J]. *IEEE Transactions on Industry Applications*, 2021, **57**(1): 814-823.
- [4] Li M Y, Huang W T, Tai N L, *et al.* A dual-adaptivity inertia control strategy for virtual synchronous generator [J]. *IEEE Transactions on Power Systems*, 2020, **35**(1): 594-604.
- [5] Mardani F, Falconar N, Shafiei N, *et al.* A digital control system for UPS systems with smart-grid capability [J]. *IEEE Journal of Emerging and Selected Topics in Power Electronics*, 2020, **8**(4): 3846-3860.
- [6] Peng Q, Fang J Y, Yang Y H, *et al.* Maximum virtual inertia from DC-link capacitors considering system stability at voltage control timescale [J]. *IEEE Journal on Emerging and Selected Topics in Circuits and Systems*, 2021, **11**(1): 79-89.
- [7] Bhowmik P, Rout P K, Guerrero J M, *et al.* Vector measurement-based virtual inertia emulation technique for real-time transient frequency regulation in microgrids [J]. *IEEE Transactions on Power Electronics*, 2021, **36**(6): 6685-6698.
- [8] Wu W H, Chen Y D, Luo A, *et al.* A virtual inertia control

- strategy for DC microgrids analogized with virtual synchronous machines [J]. *IEEE Transactions on Industrial Electronics*, 2017, **64**(7): 6005-6016.
- [9] Ren M W, Li T, Shi K, *et al.* Coordinated control strategy of virtual synchronous generator based on adaptive moment of inertia and virtual impedance [J]. *IEEE Journal on Emerging and Selected Topics in Circuits and Systems*, 2021, **11**(1): 99-110.
- [10] Yang Y, Mei F, Zhang C Y, *et al.* Coordinated adaptive control strategy of rotational inertia and damping coefficient for virtual synchronous generator [J]. *Electric Power Automation Equipment*, 2019, **39**(3): 125-131(Ch).
- [11] Karimi A, Khayat Y, Naderi M, *et al.* Inertia response improvement in AC microgrids: A fuzzy-based virtual synchronous generator control [J]. *IEEE Transactions on Power Electronics*, 2020, **35**(4): 4321-4331.
- [12] Mao Q H, Zhang Q. An improved sparrow algorithm integrating cauchy mutation and reverse learning [J]. *Computer Science and Exploration*, 2021, **15**(6):1155-1164(Ch).
- [13] Liu W, Fu J, Zhou D N, *et al.* Research on shallow neuroevolution method based on improved coyote optimization algorithm [J]. *Journal of Computer*, 2021, **44**(6): 1200-1213(Ch).
- [14] Wang F, Zhang H, Han M C, *et al.* A mixed variable multi-objective particle swarm optimization algorithm based on co-evolution to solve the problem of cooperative multi-task assignment of UAVs [J]. *Chinese Journal of Computers*, 2021, **44**(10): 1967-1983(Ch).
- [15] Wen J B, Yang J C, Wang T Y. Path planning for autonomous underwater vehicles under the influence of ocean currents based on a fusion heuristic algorithm [J]. *IEEE Transactions on Vehicular Technology*, 2021, **70**(9): 8529-8544.
- [16] Li Y G, Bai L, Zheng Z H, *et al.* Coordinated control optimization of VSG and APF for photovoltaic energy storage microgrid based on multi-objective particle swarm [J]. *Renewable Energy*, 2021, **39**(4): 541-547(Ch).
- [17] Cheng J P, Xiao J M, Wang X H. VSG control strategy based on improved particle swarm optimization algorithm [J]. *Control Engineering*, 2021, **28**(10): 2028-2037(Ch).
- [18] Yao F J, Zhao J B, Li X J, *et al.* RBF neural network based virtual synchronous generator control with improved frequency stability [J]. *IEEE Transactions on Industrial Informatics*, 2021, **17**(6): 4014-4024.
- [19] Shadravan S, Naji H R, Bardsiri V K. The Sailfish Optimizer: A novel nature-inspired metaheuristic algorithm for solving constrained engineering optimization problems [J]. *Engineering Applications of Artificial Intelligence*, 2019, **80**: 20-34.

□